Supplement of Clim. Past, 19, 1891–1904, 2023
https://doi.org/10.5194/cp-19-1891-2023-supplement

Climate of the Past
Open Access

Supplement of

Contribution of lakes in sustaining the Sahara greening during the mid-Holocene

Yuheng Li et al.

Correspondence to: Yuheng Li (yuheng@rainbow.iis.u-tokyo.ac.jp)

Table S1.

Table S1 Lake Maps

Lake Maps	Spatial resolution of original lake reconstruction	Description	Reference
LK_98 (small-lake map)	160 km	Holocene small-lake fraction derived from paleo-ecological reconstructions	(Hoelzmann, Jolly et al., 1998)
LK_02 (potential maximum-lake map)	160 km	mid-Holocene maximum-lake fraction derived using the hydrological routing algorithm (HYDRA)	(Tegen, Harrison et al., 2002)
LK1, LK2, LK3, LK4	15 arc-second	RFM2 model results on the wetlands of North Africa during the mid-Holocene corresponding to the four different rainfall types (LK1-4). The LK1 and LK2 are derived from IPSL-CM6A-LR mid-Holocene simulation; LK3 and LK4 are based on EC-Earth mid-Holocene simulation	(Chen, Ciais et al., 2021)

Considering the different spatial resolutions of the above datasets, the input lake maps have been upscaled into T42 spatial resolutions by calculating the lake area grid proportion in each T42 grid in North Africa Areas. Besides, this study used the same LK_98 and LK_02 maps as that of Specht, Claussen et al. (2022), which have been published in *http://hdl.handle.net/21.11116/0000-0009-63B5-B*.

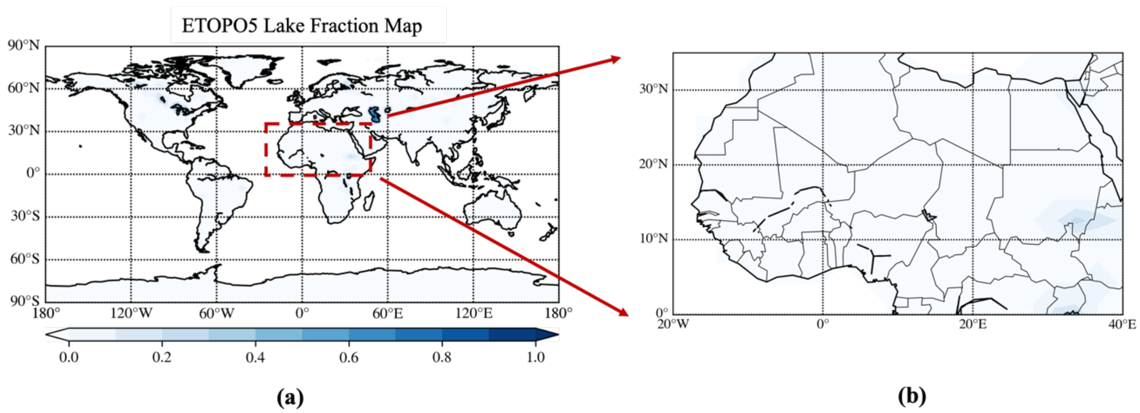

Figure S1. The (a) global prescribed lake map for mid-Holocene (MH) and pre-industrial (PI) reference experiments (ETOPO5). (b) Focus over North Africa.

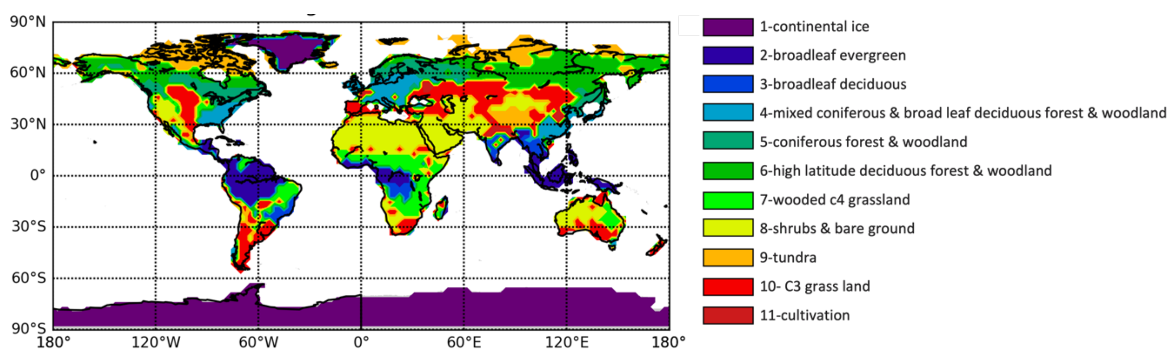

Figure S2. Vegetation type distribution map for all the experiments.

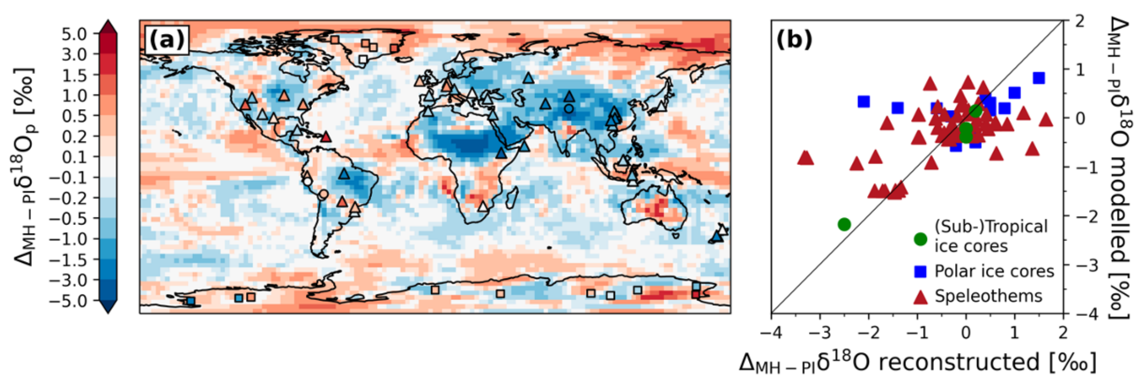

Figure S3. Isotope model-data comparison for the reference mid-Holocene simulation. The subplot (a) shows the simulated global pattern of annual mean $\delta^{18}O_p$ changes in precipitation between the MH_{ref} and PI_{ref} climate (background colors) and the observed $\delta^{18}O$ changes in polar (squares) and (sub)tropical (dots) ice cores and in calcite speleothems. The subplot (b) is a scatter plot showing a comparison of observed $\delta^{18}O$ changes from ice cores and speleothems vs. with simulated MH–PI $\delta^{18}Op$ anomalies at the same location.

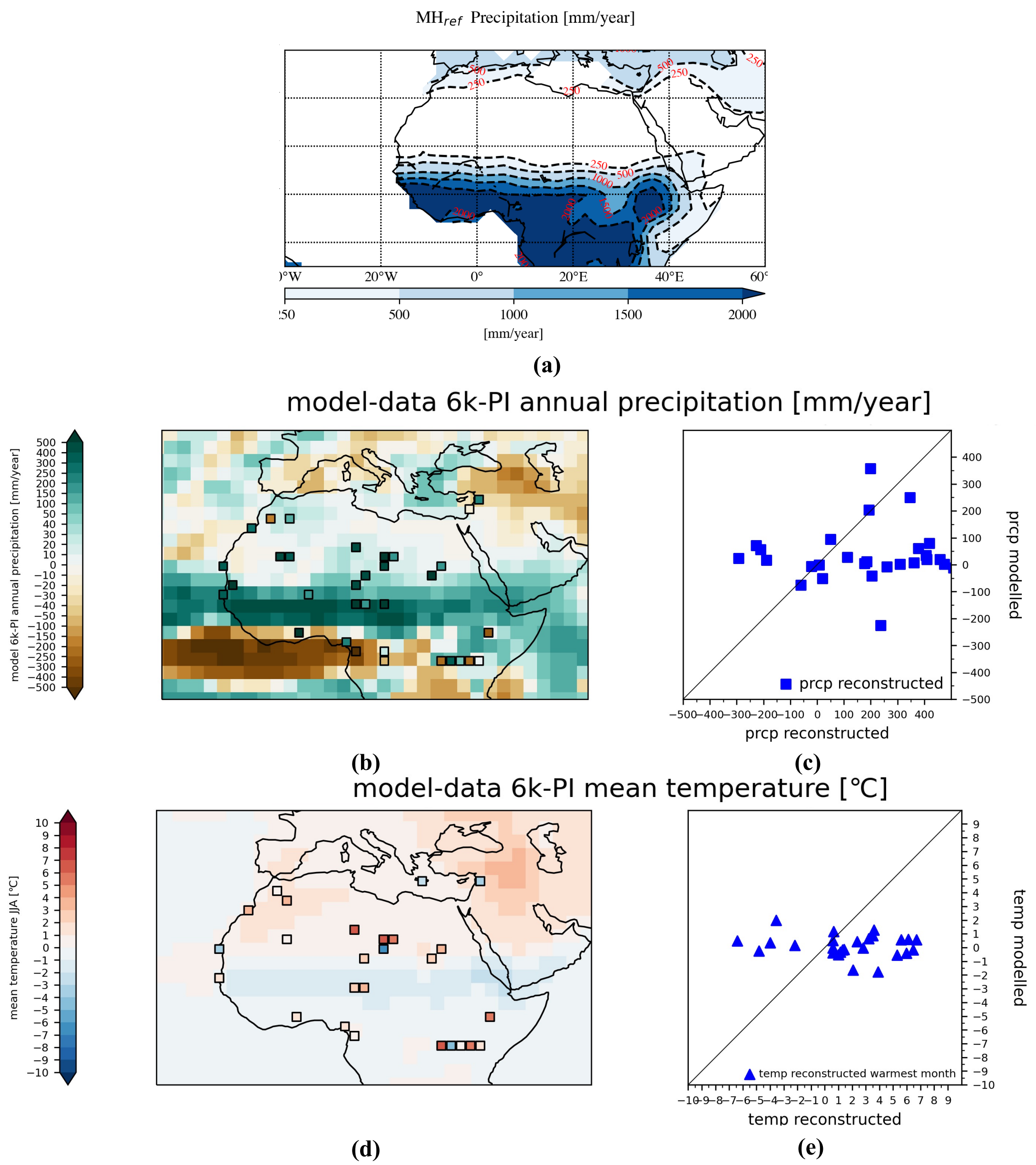

Figure S4. Precipitation and temperature model-data comparison for the reference mid-Holocene simulation in North Africa. (a) The spatial annual precipitation for MH_{ref}. (b) shows the simulated global pattern of annual mean precipitation between the MH_{ref} and PI_{ref} climate (background colors) and the observed annual mean precipitation changes (squares) between MH_{ref} and the present climate. (c) is a scatter plot showing a comparison of observed precipitation changes with simulated precipitation anomalies at the same location. (d) and (e) are the same as (b) and (c) but for the seasonal mean temperature model [Summer (JJA)]-data [warmest month] comparison.

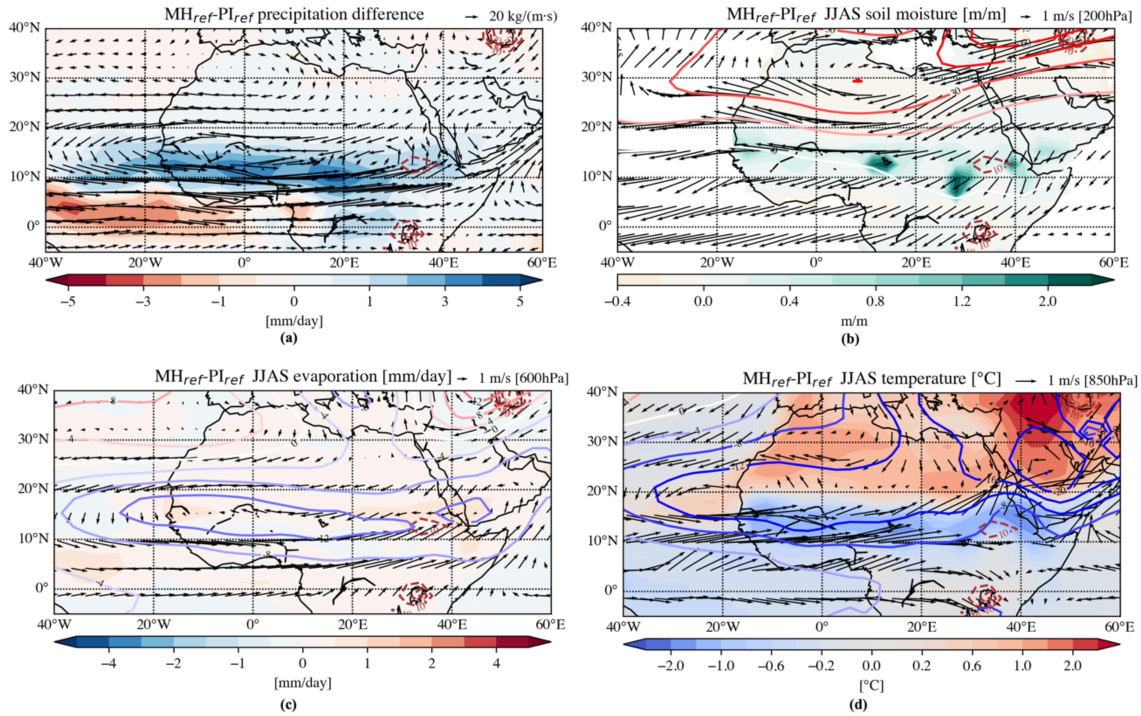

Figure S5. Simulated climatological mean anomalies between MH$_{ref}$ and PI$_{ref}$ in JJAS: (a) precipitation (shades) and the integrated vapor transportation anomalies (IVT; arrows); (b) soil moisture (shades) with 200 hPa wind (arrows) and geopotential height (contours); (c) evaporation (shades) with and 600 hPa horizontal wind and geopotential height; (d) surface temperature (shades) with 850 hPa horizontal wind, and geopotential height. For (a)-(d), the lake fraction [%] contours of the respective lake sensitivity experiment are shown with the red dashed lines, and the respective reference scale for the arrow is shown at the right top of each panel.

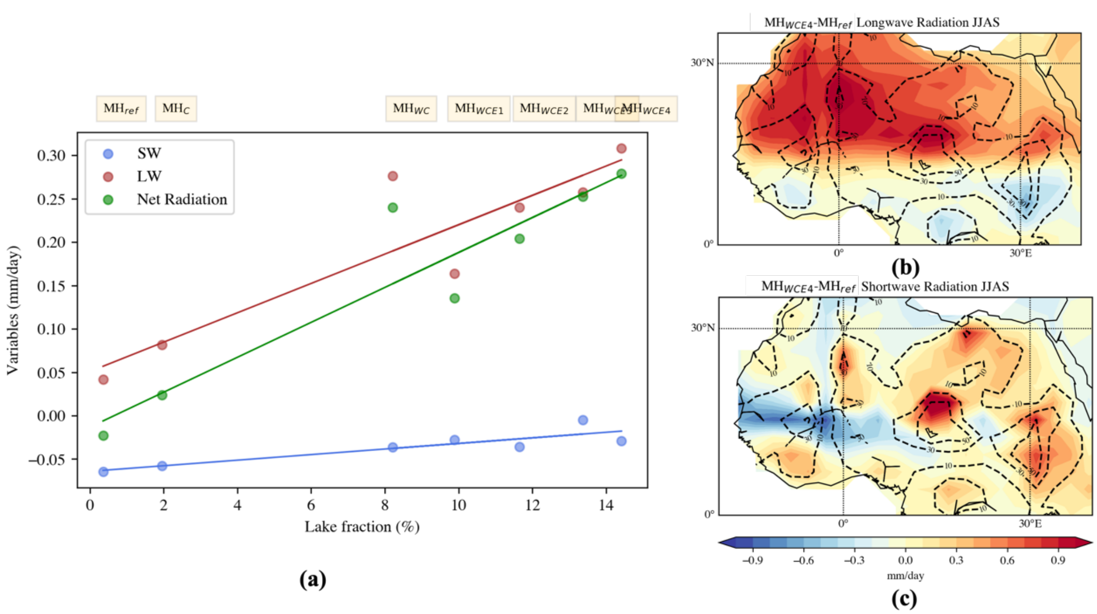

Figure S6. (a) Statistical relationship between regionally averaged radiation variables anomaly and averaged grid lake fraction over Northern Africa (20°W–40°E, 0–35°N) for MH lake experiments anomalies (relative to PI_{ref}) on the annual (circle) averages. The radiation variables include net surface shortwave radiation (blue), net surface longwave radiation (red), and net radiation (green). Simulated mid-Holocene climatological JJAS mean anomalies MH_{WCE4} with respect to MH_{ref}: (b) net surface longwave radiation (shades), (c) net surface shortwave radiation (shades). For maps (b) and (c), The lake fraction [%] contours of the respective lake sensitivity experiment are shown with the black dashed lines. All the radiations units has been transferred from [W/m^2] to [mm/day] based on the equation: $W/m^2 = 1000(kg/m^3) \times 2.5\times10^6(J/kg) \times 1mm/day\ (1/86400)(day/s) \times (1/1000)(mm/m)$.

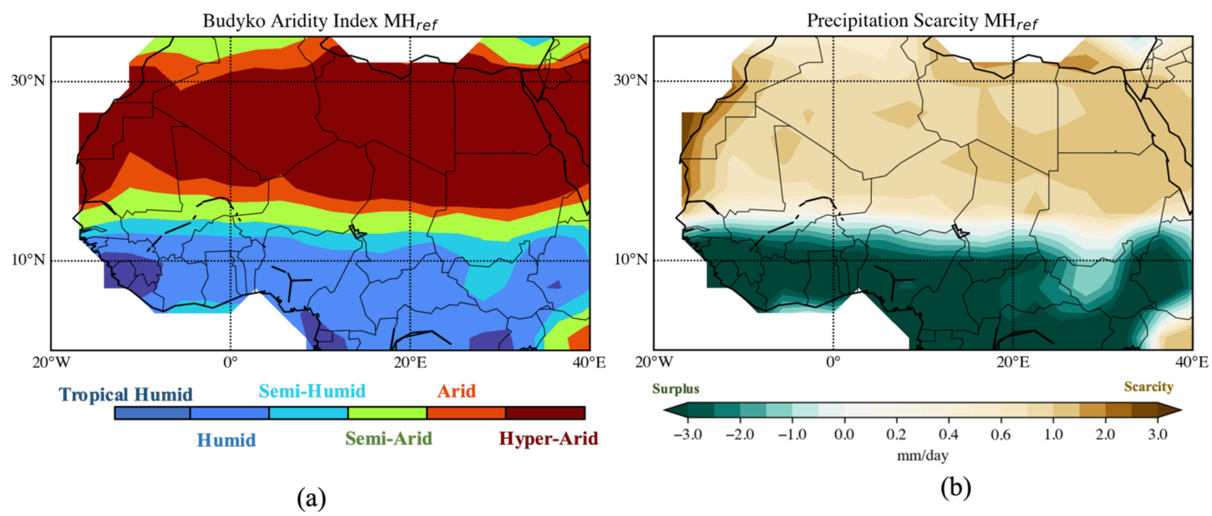

Figure S7. (a) Spatial distribution of six climate regions and (b) Spatial distribution of precipitation scarcity and precipitation surplus over Northern Africa for MH_{ref} experiments.

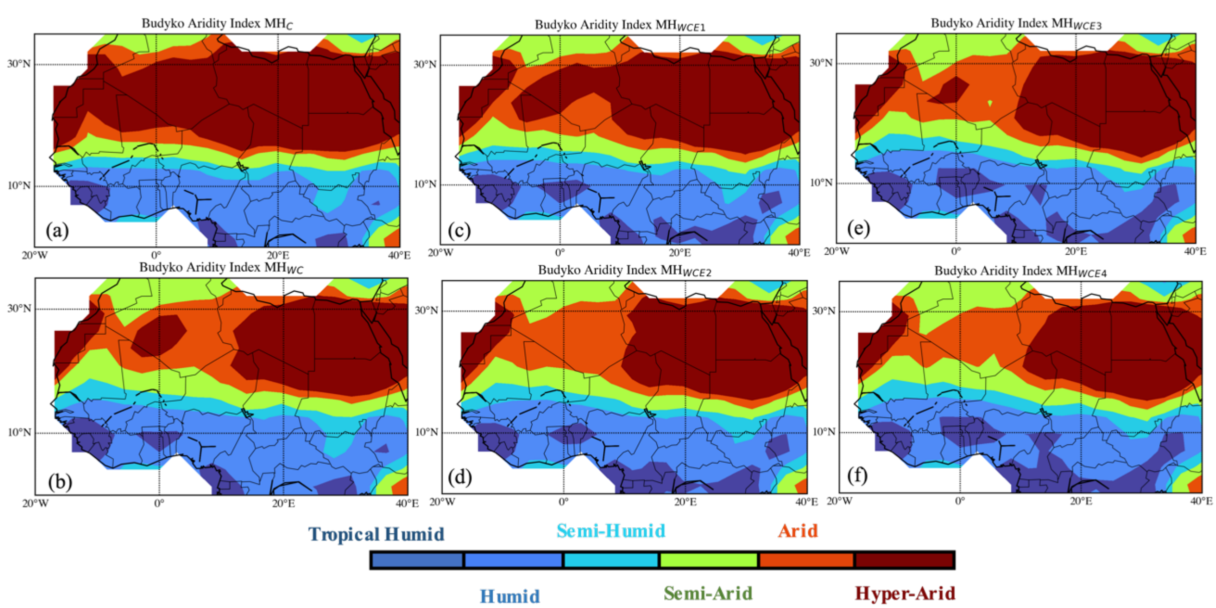

Figure S8. Spatial distribution of six climate regions for MH_C, MH_{WC}, MH_{WCE1}, MH_{WCE2}, MH_{WCE3}, and MH_{WCE4} experiments. The climate zones are classified with Budyko Aridity index (I) and precipitation (P) in Northern Africa: Tropical Humid ($I \leqslant 0.7$ and $P > 2{,}000$ mm/yr), Humid ($0.7 < I \leqslant 1.2$), Semi-Humid

(1.2 < I ⩽ 2.0), Semi-Arid (2.0 < I ⩽ 4.0), Arid (4.0 < I ⩽ 6.0) and Hyper-Arid (6.0 < I). For Budyko Aridity index calculation, see the main text in method detail.

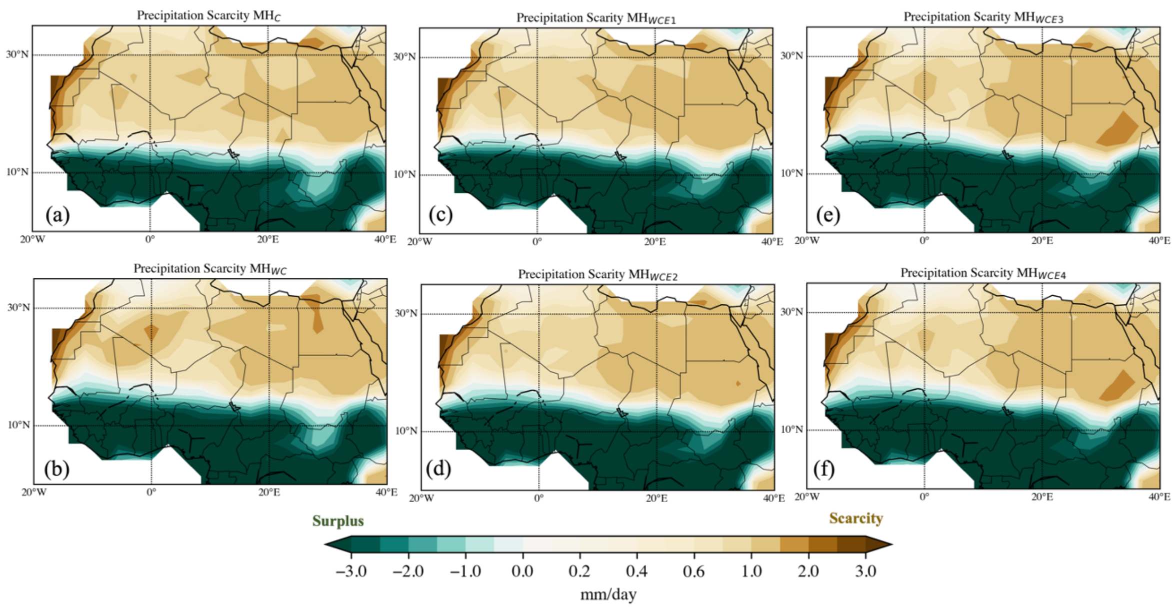

Figure S9. Spatial distribution of precipitation scarcity and precipitation surplus over Northern Africa for all the mid-Holocene experiments.

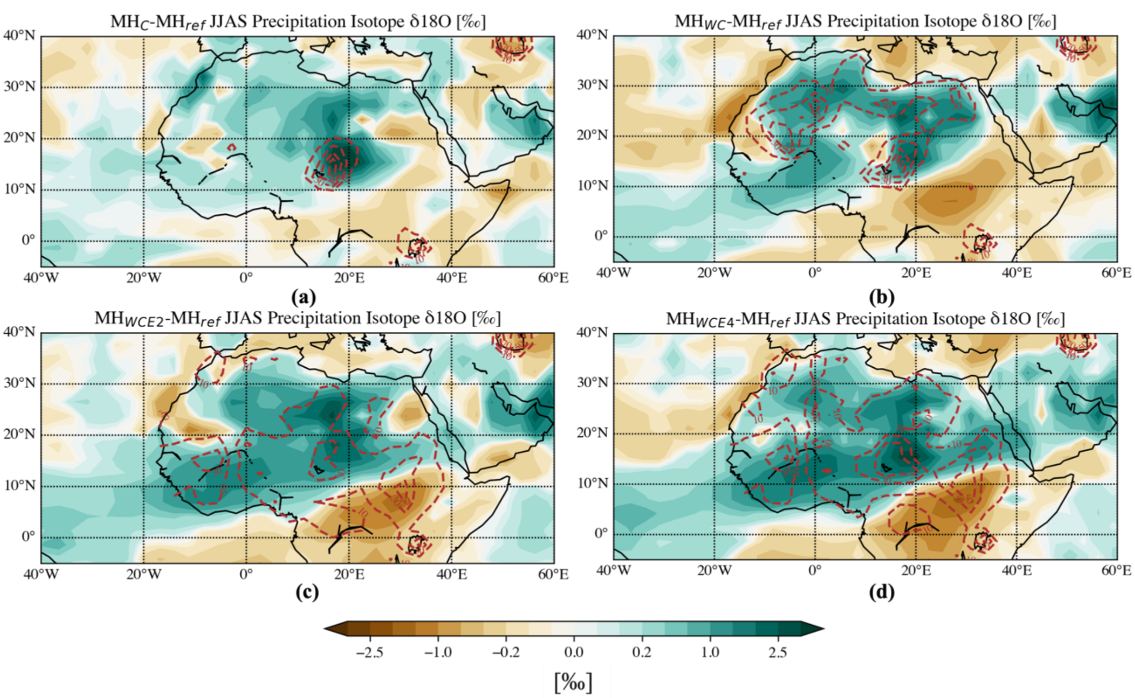

Figure S10. Changes in the stable isotope ratio $\delta^{18}O$ [‰] in precipitation for our mid-Holocene sensitivity experiments relative to MH_{ref}: (a) the climatological $\delta^{18}O$ anomaly for MH_98 experiments. (b), (c) and (d) are the same as (a) but for the MH_{WC}, MH_{WCE2} and MH_{WCE4} experiments, respectively. For (a)-(d), the lake fraction [%] contours of the respective lake sensitivity experiment are shown with the red dashed lines.

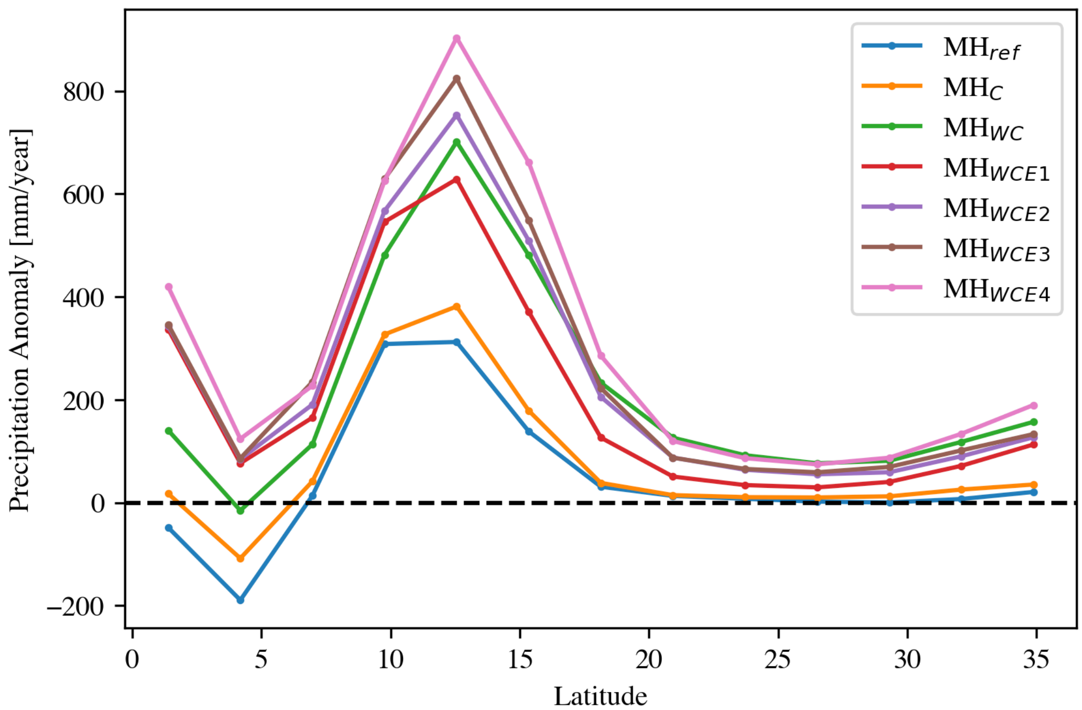

Figure 11. Zonal means, over "North Africa" land [-20°W-35°E, 0-35°N] of annual precipitation anomalies of the mid-Holocene experiments with respect to PI$_{ref}$.

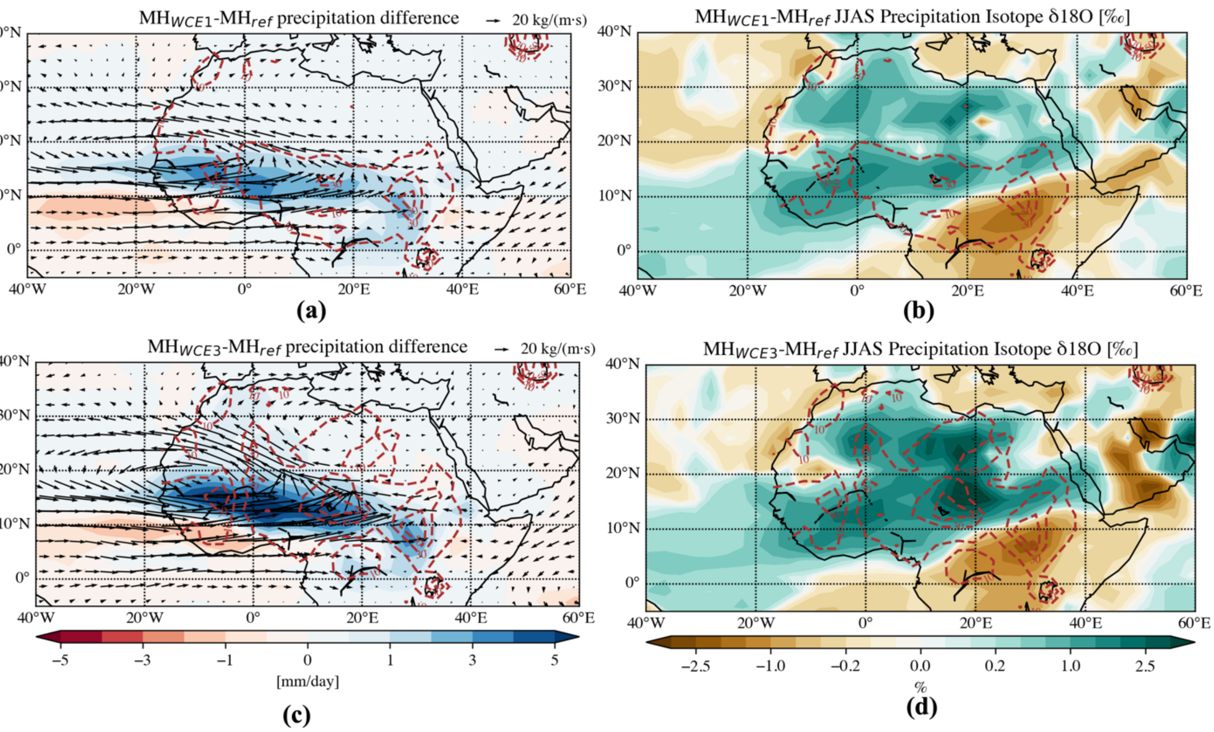

Figure S12. Anomalies relative to MH$_{ref}$ in simulated mid-Holocene climatological summer mean (June-July-August-September, JJAS) precipitation (shades) and integrated vapor transportation (IVT; arrows) for (a) MH$_{WCE1}$ and (c) MH$_{WCE3}$ experiments, respectively. Changes in the stable isotope ratio δ^{18}O [‰] in precipitation for our mid-Holocene sensitivity experiments relative to MH$_{ref}$: (a) the climatological δ^{18}O anomaly for MH$_{WCE1}$ experiments. (b) is the same as (a) but for the MH$_{WCE3}$. For (a)-(d), the lake fraction [%] contours of the respective lake sensitivity experiment are shown with the red dashed lines (contour spacing: 10%-30%-50%-70%-100%), and the respective reference scale for the arrow is shown at the right top of each panel.

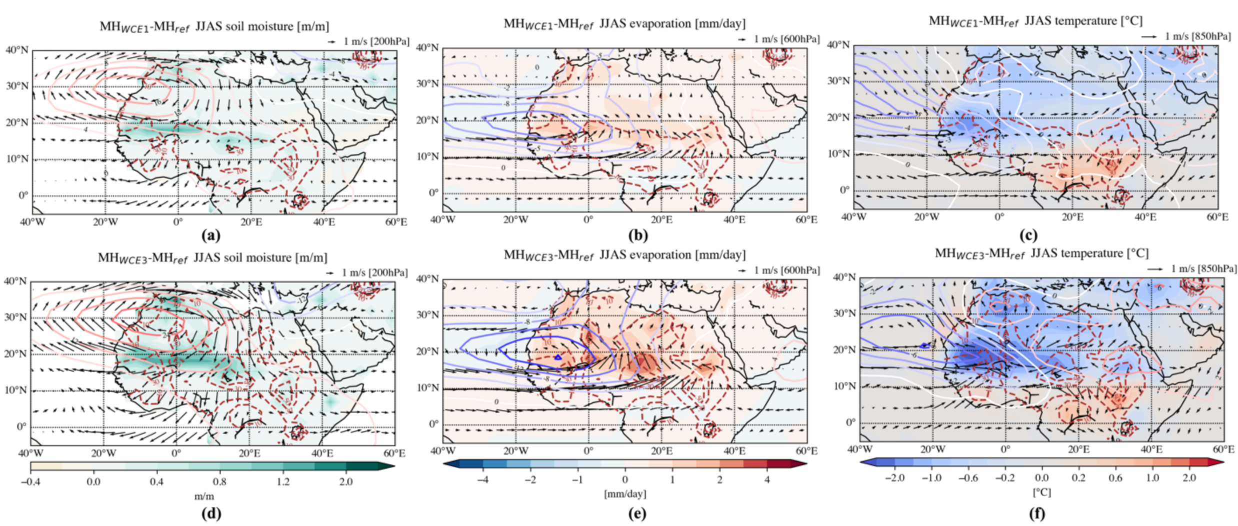

Figure S13. Simulated mid-Holocene climatological JJAS mean anomalies with respect to MH$_{ref}$: (a) soil moisture (shades) with 200 hPa wind (arrows) and geopotential height (contours), (b) evaporation (shades) with 600 hPa horizontal wind and geopotential height and (c) surface temperature (shades) with 850 hPa horizontal wind, and geopotential height for MH$_{WCE1}$ experiment. Map (d), (g) and (f) are the same as (a), (b) and (c), respectively, but for MH_{WCE3} experiment. For all the maps, the lake fraction [%] contours of the respective lake sensitivity experiment are shown with the red dashed lines, and the respective reference scale for the arrow is shown at the right top of each panel.